Countergradient Momentum Transport in Clear Convective Atmospheric Boundary Layers

de Roode, Stephan R.; Jansson, Fredrik; Mak, Lydia; Nuijens, Louise

DOI
10.1029/2024MS004579

Publication date
2025

Document Version
Final published version

Published in
Journal of Advances in Modeling Earth Systems

Citation (APA)
de Roode, S. R., Jansson, F., Mak, L., & Nuijens, L. (2025). Countergradient Momentum Transport in Clear Convective Atmospheric Boundary Layers. *Journal of Advances in Modeling Earth Systems*, *17*(9), Article e2024MS004579. https://doi.org/10.1029/2024MS004579

JAMES | Journal of Advances in Modeling Earth Systems

RESEARCH ARTICLE
10.1029/2024MS004579

Countergradient Momentum Transport in Clear Convective Atmospheric Boundary Layers

Stephan R. de Roode[1], Fredrik Jansson[1], Lydia Mak[1], and Louise Nuijens[1]

[1]Faculty of Civil Engineering and Geosciences, Delft University of Technology (TU Delft), Delft, The Netherlands

Key Points:

- For convective boundary layers with wind shear we diagnose countergradient momentum transport
- In convective boundary layers with wind shear, eddy viscosity profiles for the two horizontal wind components differ significantly
- A modified solution to the Ekman spiral shows that anisotropic eddy viscosity affects the wind's turning

Correspondence to:

S. R. de Roode,
s.r.deroode@tudelft.nl

Citation:

de Roode, S. R., Jansson, F., Mak, L., & Nuijens, L. (2025). Countergradient momentum transport in clear convective atmospheric boundary layers. *Journal of Advances in Modeling Earth Systems*, *17*, e2024MS004579. https://doi.org/10.1029/2024MS004579

Received 17 JUL 2024
Accepted 17 AUG 2025

Abstract The vertical profiles of the wind speed and direction in atmospheric boundary layers are strongly controlled by turbulence. Most global weather forecast and climate models parameterize the vertical transport of horizontal momentum by turbulent eddies by means of a downgradient eddy diffusion approach, in which the same stability-dependent eddy viscosity profile is applied to both horizontal wind components. In this study we diagnose eddy viscosity profiles from large-eddy simulations of five convective boundary layers with wind shear. Each simulation was forced by the same geostrophic wind of 7.5 ms^{-1}, but with different surface heat fluxes in the range between 0.03 and 0.18 mKs^{-1}. We find that the eddy viscosity profiles for the two horizontal wind components differ significantly, in particular, we diagnose negative eddy viscosities, indicating vertical turbulent transport that is counter the mean gradient. This suggests that a purely downgradient diffusion approach for turbulent momentum fluxes is inadequate. A modified solution of the Ekman spiral demonstrates that different eddy viscosity profiles for the two horizontal wind components lead to a different wind profile. To improve parameterizations that apply a downgradient diffusion approach for momentum, correction terms to allow for non-local, boundary-layer scale transport should be incorporated.

Plain Language Summary During the day, especially when the ground heats up, the air near the surface becomes turbulent. This turbulence, which we often feel as gusty winds or see as rising warm air, moves slower-moving air upward and faster-moving air downward. This process affects both how fast the wind blows and the direction it takes. Because turbulence happens on very small scales that computers cannot fully capture, weather and climate models use simplified methods, called parameterizations, to represent it. Usually, these models assume that this turbulent mixing of air behaves the same in all horizontal directions. In our study, we used a detailed, high-resolution simulation that more accurately captures turbulent air motions. We found that the way air mixes can differ depending on the direction of the wind. In fact, the mixing strength, called eddy viscosity, can even become negative, something that standard models do not account for. To show how this matters, we updated a classic example from meteorology called the Ekman spiral, which describes how wind direction changes with height. Our findings suggest that current methods used in weather models could be improved by accounting for these directional differences in the turbulent viscosity.

1. Introduction

In the lower part of the atmosphere turbulent updrafts (downdrafts) transport low (high) horizontal momentum from just above the ground to higher levels in the atmosphere. The intensity with which horizontal momentum is being mixed by turbulence is important in shaping the vertical profile of the wind. Because global weather forecast and climate models operate at mesh sizes that are too coarse to resolve turbulence, turbulent momentum transport must be parameterized. In the atmospheric boundary layer, it is common to model turbulent momentum transport using a downgradient diffusion approach, as introduced in early general circulation model studies by Smagorinsky (1963) and Smagorinsky et al. (1965). According to the downgradient diffusion approach, the vertical turbulent transport ($\overline{w'\varphi'}$), which arises from the correlated fluctuations of the vertical wind w and an arbitrary quantity φ (e.g., momentum, heat or moisture), can be calculated as:

$$\overline{w'\varphi'} = -K_\varphi \frac{\partial \overline{\varphi}}{\partial z}, \tag{1}$$

where primes are used to indicate fluctuations with respect to the mean, K_φ represents the eddy diffusivity applied to the mean value of φ (as indicated by the overbar), or, more precisely, the eddy viscosity K_m when applied to momentum. Both K_φ and K_m are flow-dependent quantities, primarily governed by the stability of the atmosphere

in terms of wind shear and its thermal stratification. Additionally, they are assumed to be proportional to the intensity of turbulence and the size of the largest, dominant eddies.

In the European Center for Medium-Range Weather Forecasts (ECMWF) model the strength of turbulent diffusion is used as a tuning parameter to control the evolution of synoptic cyclones and anticyclones, demonstrating its large-scale impact (Sandu et al., 2013). Unfortunately, such an adjustment comes with a penalty in terms of less accurate wind profile representations. Currently, systematic biases in wind direction are found for both clear and cloud-topped boundary layers in the ECMWF model (Sandu et al., 2020), which may be rooted in the momentum tendencies by diffusive transport and moist convective transport.

The downgradient diffusion approach, according to Equation 1, has some notable flaws. For example, Holtslag and Moeng (1991) demonstrated through large-eddy simulations (LESs) that the buoyancy flux in the middle part of the convective boundary layer is counter the mean gradient. According to Equation 1, this would imply a negative value for the eddy viscosity. To maintain a positive value for the eddy viscosity, Holtslag and Moeng (1991) proposed a modification to the downgradient diffusion approach. Their modification introduces a non-local correction term γ_ϕ according to

$$\overline{w'\varphi'} = -K_\varphi\left(\frac{\partial\overline{\varphi}}{\partial z} - \gamma_\phi\right). \tag{2}$$

Frech and Mahrt (1995) and Brown and Grant (1997) also proposed incorporating a non-local term for momentum fluxes, similar to Equation 2. While Brown and Grant (1997) concluded that including a non-local term improves wind profiles in clear convective boundary layers, they noted that such an approach has little support from observations. Recently, however, important evidence of countergradient momentum fluxes was obtained from LES studies of shallow cumulus clouds conducted by Larson et al. (2019), Helfer et al. (2021), and Dixit et al. (2021).

Frech and Mahrt (1995) anticipated the existence of countergradient momentum fluxes but were unable to confirm this through observations. The present study aims to support their hypothesis using high-resolution LESs of shear-driven, clear convective boundary layers. The set-up of the simulations, which were performed at mid-latitudes where the Coriolis force plays a key role in controlling the wind, is presented in Section 2. In Section 3, we demonstrate countergradient momentum fluxes. This section also examines the effect of the surface momentum flux on wind turning, and we show that the eddy viscosity profiles for the two horizontal wind components typically differ. Section 4 presents the momentum flux budgets and explains how buoyancy influences the vertical transport of horizontal momentum. We analyze the impact of anisotropic eddy viscosity on wind turning by deriving a modified solution for the Ekman wind spiral in Section 5. Section 6 addresses the implications of these findings for momentum flux parameterizations. Finally, Section 7 provides a summary of the study and offers recommendations.

2. Setup of the Large-Eddy Simulations

Numerical experiments were performed using the Dutch Atmospheric Large-Eddy Simulation (DALES) model. A comprehensive explanation of the model can be found in Heus et al. (2010); therefore, only a brief description is provided here. This section also outlines the details of the case setups.

2.1. Model Description

LES models solve the conservation equations for filtered variables, denoted by a tilde. The filtered, anelastic momentum equation is given by,

$$\frac{\partial\widetilde{u_i}}{\partial t} + \frac{1}{\rho_0}\frac{\partial\rho_0\widetilde{u_i}\widetilde{u_j}}{\partial x_j} = \beta\delta_{i3}\left(\widetilde{\theta_v} - \overline{\theta_v}\right) - \frac{\partial\pi}{\partial x_i} - \frac{1}{\rho_0}\frac{\partial\rho_0\tau_{ij}}{\partial x_j} + \tilde{S}_{u_i}, \tag{3}$$

with t the time, the velocity vector components $(u_1, u_2, u_3) = (u, v, w)$ in the (x, y, z) direction, respectively, $\beta = g/\theta_0$ the thermal expansion factor for air, g the gravitational acceleration, $\rho_0(z)$ and $\theta_0(z)$ are the height-dependent reference state density and virtual potential temperature, respectively, δ_{ij} denotes the Kronecker-delta function, the virtual potential temperature is defined as,

$$\theta_v \equiv \theta(1 + \epsilon_I q_v), \tag{4}$$

with q_v the water vapor specific humidity, $\epsilon_I \approx 0.608$ a thermodynamic constant, π is the modified pressure (Deardorff, 1973) and an overbar is used to indicate a horizontal slab-mean value. For compact notation we have included the mean horizontal pressure gradient and the Coriolis force in the source function S_{u_i}. DALES also solves prognostic equations for scalars like the liquid water potential temperature θ_l and the total water specific humidity q_t. In the absence of a source term the prognostic equation for a filtered arbitrary scalar $\varphi \in \{\theta, q\}$ is given by

$$\frac{\partial \tilde{\varphi}}{\partial t} + \frac{1}{\rho_0}\frac{\partial \rho_0 \tilde{u}_j \tilde{\varphi}}{\partial x_j} = -\frac{1}{\rho_0}\frac{\partial \rho_0 \widetilde{u_j'' \varphi''}}{\partial x_j}, \tag{5}$$

where following Heus et al. (2010) the double primes denote subfilter-scale fluctuations. However, as we will consider only conditions without moisture, $q_t = 0$, the liquid potential temperature θ_l becomes equal to both the potential and virtual potential temperatures, $\theta_l = \theta = \theta_v$.

The deviatoric part of the subfilter-scale momentum flux τ_{ij} is computed from Deardorff (1980),

$$\tau_{ij} \equiv \widetilde{u_i u_j} - \widetilde{u}_i \widetilde{u}_j - \frac{2}{3}\delta_{ij}\tilde{e} = -K_m\left(\frac{\partial \tilde{u}_j}{\partial x_i} + \frac{\partial \tilde{u}_i}{\partial x_j}\right). \tag{6}$$

The eddy viscosity K_m was computed from the full prognostic equation for subgrid turbulent kinetic energy (TKE), represented as e, following Deardorff (1980). This method employs a constant length scale ℓ, which is directly proportional to the mesh sizes in all three spatial directions and is defined by $\ell = (\Delta x \Delta y \Delta z)^{1/3}$, to give $K_m = c_m \ell e^{1/2}$, with c_m a proportionality constant. The value of the latter, and other constants used in DALES are summarized by De Roode et al. (2017).

2.2. Set-Up of the Cases

The simulations of five convective boundary layers were configured identically to the studies by Sullivan and Patton (2011) and Salesky et al. (2017). The potential temperature θ in the boundary layer was set to a constant value of 300 K up to its top at a height h at 1 km. Above this height, θ increased by 8 K across the thermal inversion layer, which had an initial thickness of 100 m. The free troposphere has a stable potential temperature vertical gradient of 3 $\mathrm{Kkm^{-1}}$. The atmospheric moisture was set to zero. Each simulation applied a different, constant surface heat flux $\overline{w'\theta'}_{sfc}$, with values of 0.03, 0.07, 0.1, 0.14, and 0.18 $\mathrm{mKs^{-1}}$, respectively. In all simulations, turbulence was triggered by adding random perturbations to the potential temperature field in the range between −0.1 and 0.1 K, and by prescribing an initial subgrid TKE value of 1 $\mathrm{m^2 s^{-2}}$ within the boundary layer.

The horizontal domain size was set to $12 \times 12\ \mathrm{km^2}$ using 512×512 grid points, and the vertical resolution was set to 12.5 m. The vertical domain size varied from 2 km up to 3.5 km for the simulations with the smallest and largest surface heat flux values, respectively. The increased vertical domains accommodate boundary-layer growth due to entrainment and ensure that turbulent eddies remain well below the sponge layer in which fluctuations of velocity and scalars are damped. This artificial damping layer, in our simulations the upper 25% of the vertical domain size, is applied to prevent spurious reflection of waves at the top of the model domain (Heus et al., 2010).

Instead of using large-scale horizontal pressure gradients as a forcing condition, DALES prescribes the geostrophic winds U_g and V_g, defined as:

$$U_g \equiv -\frac{1}{\rho f}\frac{\partial P}{\partial y}, V_g \equiv \frac{1}{\rho f}\frac{\partial P}{\partial x}, \tag{7}$$

with P denoting the large-scale pressure and ρ the air density, the horizontal pressure gradients are expressed in terms of the geostrophic wind components. A set of reference simulations was subjected to constant geostrophic wind forcings, specifically $U_g = 7.5$ and $V_g = 0$ ms^{-1}, with the Coriolis parameter set to $f = 1.0 \times 10^{-4}$s^{-1}, corresponding to a latitude of 43.4°N. Following Salesky et al. (2017), the roughness length was set to $z_0 = 0.10$ m. The same value for the roughness length was used by Brown and Grant (1997) in their LES study on momentum transport in convective boundary layers.

The original version of this study presented results that were obtained with a stronger geostrophic wind, $U_g = 15$ ms^{-1} (De Roode et al., 2024). Since this forcing is relatively strong and could be considered as an uncommon atmospheric condition, we re-ran all the simulations with the geostrophic wind reduced to $U_g = 7.5$ ms^{-1}. We found that both sets of simulations produced qualitatively similar results.

To ensure that the LES results, most notably those exhibiting a countergradient momentum flux regime, are not due to the specific choices of the geostrophic wind direction and roughness length value, we performed sensitivity experiments for the case with a surface heat flux of 0.1 mKs^{-1}. In the first set we performed two additional simulations with reduced surface roughness length values down to 0.01 and 0.001 m, respectively. In a second set of sensitivity experiments we systematically increased the angle of the geostrophic wind vector in increments of 10° from the reference run value of 0 up to 90°.

The simulations did not incorporate forcings such as large-scale advection of momentum or heat. In DALES, vertical gradients of the prognostic variables in the lowest model layer are obtained by application of Monin-Obukhov similarity relations. For numerical stability reasons, an adaptive time step was employed, based on the maximum values of the Courant and Péclet numbers in the model domain.

The simulations were conducted using both a second-order advection scheme and a monotonic "kappa" scheme (Vreugdenhil & Koren, 1993). This paper presents results obtained exclusively with the kappa scheme, as it avoids numerical overshoots through the thermal inversion, which can cause spurious turbulence in the free troposphere (Bretherton et al., 1999). It is important to note that the choice of the advection scheme does not significantly impact our analysis.

2.3. Diagnostics

Every 60 s, slab-mean statistics were diagnosed. These fields were then time-averaged over 10-min intervals before being saved. Following Reynolds decomposition, horizontal slab-mean values will be denoted with capitals for mean-state variables, and fluctuations with primes, like $u = U + u'$. This technique was applied to the resolved fields to compute resolved fluxes, variances, and third-order moments, as well as horizontal slab-mean vertical subfilter-scale fluxes. Unless otherwise stated, we present total vertical turbulent fluxes of momentum and heat, which include both resolved and subgrid contributions. It is worth noting that above the surface layer the ratio of subfilter to total momentum flux is small.

In the subsequent analyses of the results, several velocity and length scales will be employed. The surface friction velocity is defined as:

$$u_* = \left(\overline{u'w'}_{\mathrm{sfc}}^2 + \overline{v'w'}_{\mathrm{sfc}}^2\right)^{1/4}, \tag{8}$$

where the subscript "sfc" denotes the ground surface value. The convective velocity scale was computed from

$$w_* = \left(\beta \overline{w'\theta'}_{\mathrm{sfc}} h\right)^{1/3} \tag{9}$$

where h is the depth of the boundary layer diagnosed from the height where the vertical gradient of the mean potential temperature has its maximum value. Additionally, a velocity scale w_m will be applied, combining the surface friction and convective velocity scales according to Brown et al. (2006),

$$w_m = \left(u_*^3 + 0.25 w_*^3\right)^{1/3}. \tag{10}$$

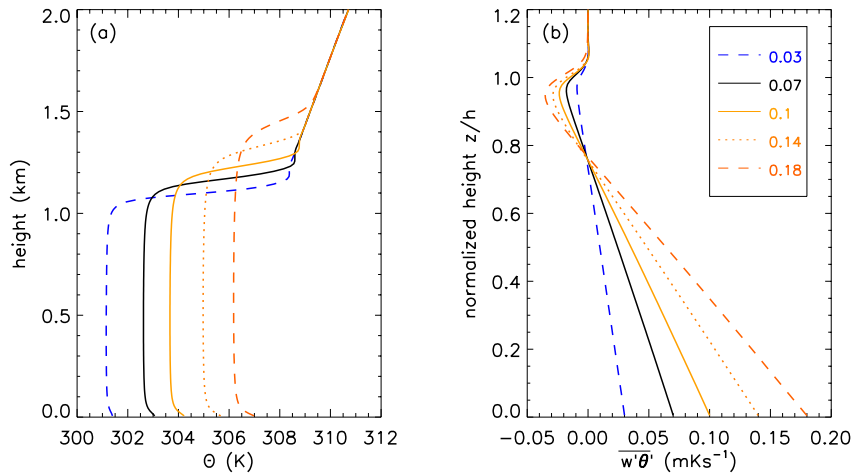

Figure 1. Hourly averaged horizontal slab-mean values of (a) the potential temperature as a function of height and (b) the vertical turbulent flux of potential temperature as a function of height normalized by the boundary layer depth. The results correspond to the 8th hour of the simulations. The legend indicates the surface heat flux, $\overline{w'\theta'}_{sfc}$, in units of Kms^{-1}.

3. Large-Eddy Simulation Results of Wind and Momentum Transport in Atmospheric Boundary Layers

Here we analyze the LES results with a focus on the horizontal mean vertical profiles of the horizontal wind and turbulent momentum fluxes. Specifically, we demonstrate that for cases driven by a positive surface buoyancy flux and wind shear, the momentum flux becomes countergradient.

We mainly present results representing horizontal slab-mean values obtained during the 8th hour of the simulations. To demonstrate that some key findings are not dependent on this specific time period, time series are also included. To facilitate a quick and easy comparison of the simulation results, most plots show results as a function of the height normalized by the hourly mean inversion height.

3.1. Mean State and Turbulent Fluxes

Figure 1a illustrates the impact of the surface boundary condition on the potential temperature and the depth of the boundary layer. All convective boundary layers with shear exhibit a vertically well-mixed structure. A stronger surface heat flux promotes faster boundary layer growth by enhancing heating through entrainment of relatively warm air from above the thermal inversion into the boundary layer. This is further demonstrated in Figure 1b, which shows negative values of $\overline{w'\theta'}$ near the top of the boundary layer, indicating downward (upward) turbulent transport of warm (cold) air.

The minimum value of $\overline{w'\theta'}$ at the top of the boundary layer is commonly accepted to be a fixed fraction of its surface value, typically $\eta \approx 0.2$. However, this value can vary slightly with the thickness of the inversion layer (VanZanten et al., 1999). Rapid boundary layer growth tends to smooth out the minimum value of the heat flux, making it appear somewhat smaller. In convective boundary layers, the entrainment velocity, w_e, depends on the surface heat flux and the jump of the potential temperature across the inversion layer, $\Delta\Theta$, following

$$w_e = \eta \frac{\overline{w'\theta'}_{sfc}}{\Delta\Theta}. \tag{11}$$

Pino et al. (2003) found that η increases in the presence of wind shear across the inversion layer. Under horizontally homogeneous conditions, the growth rate of the boundary layer depth is given by

$$\frac{dh}{dt} = w_e + \overline{w}_{subs}. \tag{12}$$

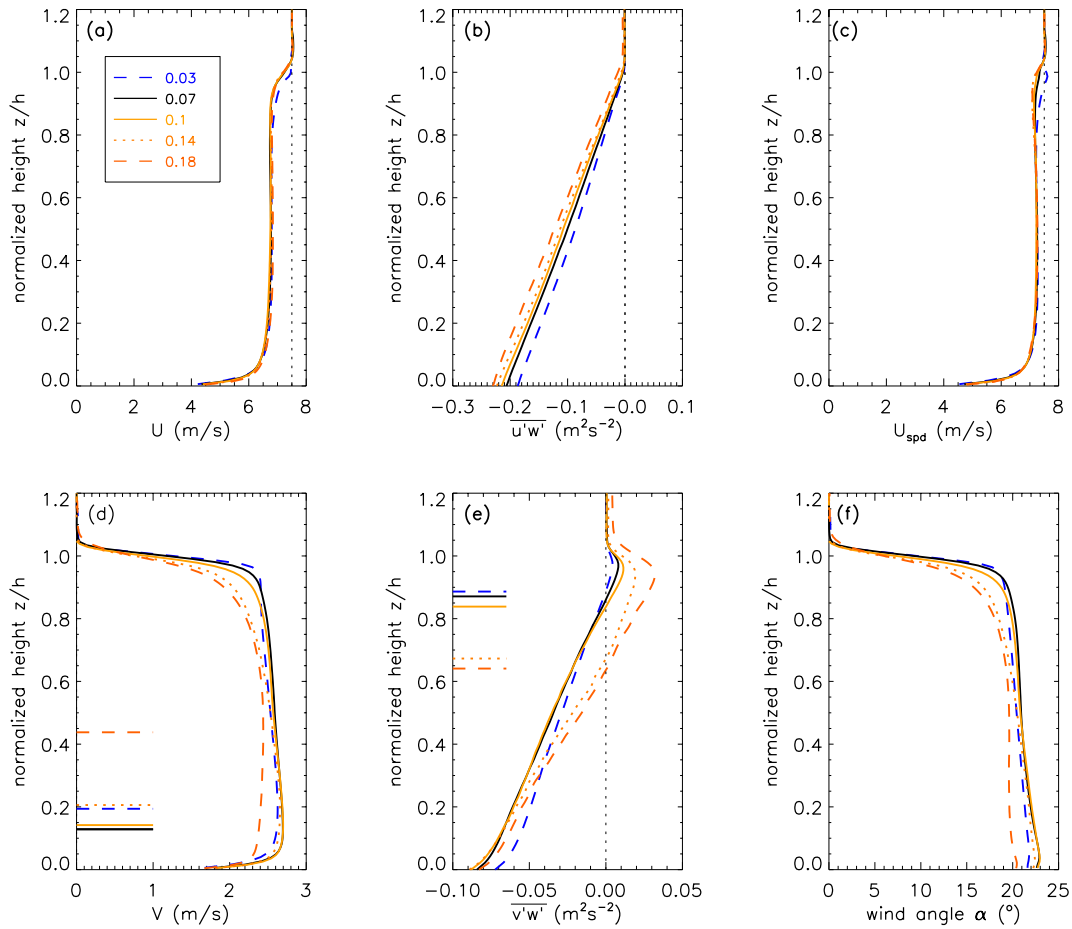

Figure 2. Vertical profiles of the horizontal wind components (a) U, (d) V, (c) the wind speed U_{spd}, (b) the momentum flux $\overline{u'w'}$, (e) $\overline{v'w'}$, and (f) the wind direction. The results represent horizontal slab-mean values averaged over the 8$^{\text{th}}$ hour of the simulations. The fluxes represent the total of the resolved and subgrid flux contributions. Heights are normalized by the boundary layer height h. The thin dotted vertical lines in panels (a) and (c) indicate the geostrophic winds, while in panels (b) and (e) they indicate the zero line. The short horizontal lines in panel (d) denote the heights where the vertical gradient of V changes sign, and in panel (e), the heights at which the momentum flux $\overline{v'w'}$ changes sign, respectively. The maximum values of V are all obtained in the lower part of the boundary layer, with some of them almost at the same (normalized) height.

In the absence of large-scale subsidence ($\overline{w}_{\text{subs}} = 0$), the growth rate of the boundary layer depth depends solely on the entrainment velocity. Since all cases started with the same initial value for $\Delta\Theta$, the differing growth rates of the convective boundary layers can be attributed entirely to variations in surface heat flux values.

3.2. Countergradient Momentum Flux Regime

Figure 2d illustrates that turbulent convection tends to homogenize the vertical profiles of the wind speed $U_{\text{spd}} = \left(U^2 + V^2\right)^{1/2}$ to a state that varies only weakly with height within the bulk of the boundary layer. Except for the case with the largest surface heat flux the height where the cross-isobaric wind component V has a local maximum, as indicated by the horizontal lines, is present in the lower part of the boundary layer, similar to the findings presented by Salesky et al. (2017) in their Figure 3b. A similar peak in the meridional wind at a relatively low height was also found from LESs of trade-wind cumulus clouds (Stevens et al., 2001).

Figure 2b shows that the momentum flux $\overline{u'w'}$ profiles vary almost linearly from a negative value near the ground to zero values near the top of the boundary layer. By contrast, as indicated by the horizontal lines, the values for $\overline{v'w'}$ change sign within the boundary layer. The $\overline{v'w'}$ profiles tend to cross the zero line relatively close to the top of the boundary layer. The flux $\overline{v'w'}$ has some small but positive values near the top of the boundary layer,

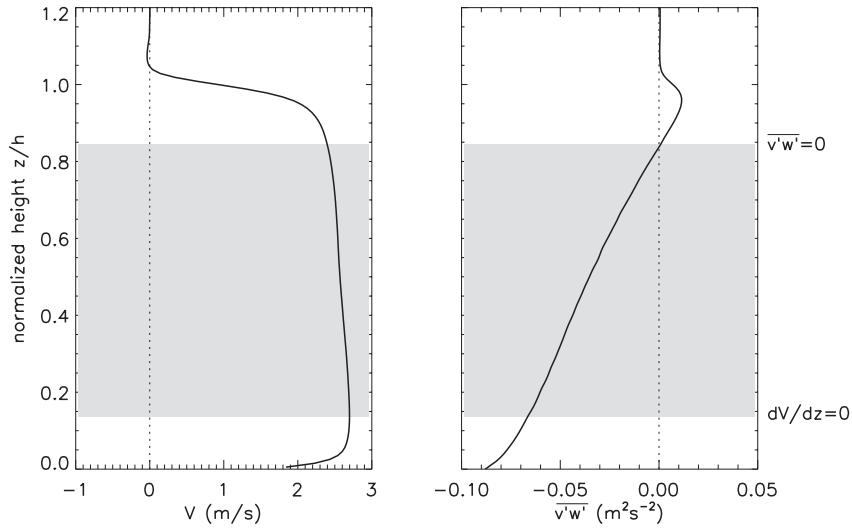

Figure 3. Vertical profiles of V and $\overline{v'w'}$ for the case with a surface heat flux $\overline{w'\theta'}_{sfc} = 0.1$ mKs^{-1}. The results represent hourly mean values obtained during the 8th hour of the simulation. The gray band highlights the countergradient flux regime, delimited by heights where $\partial V/\partial z = 0$ and $\overline{v'w'} = 0$.

consistent with a positive entrainment velocity and a negative jump ΔV, which indicates an upwards (downwards) transport of relatively large (small) values of v. For boundary layers with a sharp and thin inversion layer, the flux of any quantity at the top of the boundary layer is controlled by the entrainment velocity w_e and the jump of φ at the top of the boundary layer $\Delta\varphi$, known as the flux-jump relation (Lilly, 1968),

$$\overline{w'\varphi'}_h = -w_e\Delta\varphi. \tag{13}$$

The increasing positive values of $\overline{v'w'}$ at the boundary-layer top for increasing surface heat flux thus signify a stronger entrainment flux of momentum. According to Equation 11 this can be explained partly from the fact that w_e is proportional to $\overline{w'\theta'}_{sfc}$, but also because a stronger heating of the boundary layer tends to reduce the inversion jump of $\Delta\Theta$ (see Figure 1a), which also tends to enhance w_e.

Figure 3 shows the layer between the maximum value for V, which is present at a relatively low height, and the height at which $\overline{v'w'}$ changes sign, rather close to the top of the boundary layer. In this gray-shaded band both $\partial V/\partial z$ and $\overline{v'w'}$ have a negative value, which demonstrates that $\overline{v'w'}$ is countergradient. An inspection of Figure 2d and e shows that a countergradient regime for $\overline{v'w'}$ is clearly present for all cases. The wind U is almost vertically well mixed. However, a weak local maximum value can develop in the upper part of the boundary layer, which also leads to a weak countergradient flux. This will be explained in more detail in Sections 4 and 5.

De Roode et al. (2004) explain that countergradient transport can be expected if the mean vertical gradient of an arbitrary quantity, $\partial\overline{\varphi}/\partial z$, changes sign within the boundary layer. To satisfy pure downgradient transport, its vertical turbulent flux $\overline{w'\phi'}$ should change sign at exactly the same height, a constraint that is often not met. The boundary conditions of the cross-isobaric wind component, namely $V = 0$ at $z = 0$ (no-slip) and $z > h$ (for $V = V_g = 0$), dictate that its vertical gradient must change sign in the boundary layer, particularly since turbulent momentum transport will produce a finite cross-isobaric wind component (see Svensson & Holtslag, 2009, their Equation 3). This finding illustrates that countergradient transport does not only occur in fields of shallow cumulus clouds (Dixit et al., 2021; Larson et al., 2019), but can also be present in commonly observed clear convective boundary layers with shear.

To demonstrate the presence of a persistent countergradient momentum flux regime for $\overline{v'w'}$, Figure 4 shows the mean normalized heights at which the vertical gradient of V changes sign and where $\overline{v'w'} = 0$. These quantities were computed from 10-min mean vertical profiles, and the figure presents their averages and standard deviations over an 8-hr simulation period. In all cases, the mean height at which V reaches its maximum lies in the lower part

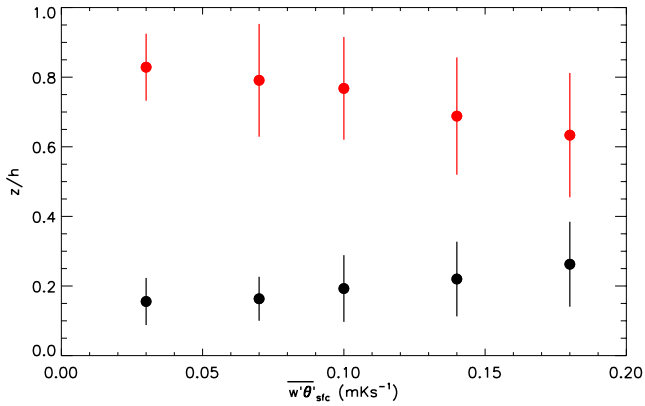

Figure 4. The countergradient momentum flux regime for the five convective boundary layers with wind shear. The filled circles represent the time-mean values of the normalized heights where the horizontal slab-mean wind V reaches its maximum value (black), and at which $\overline{v'w'} = 0$ (red). The vertical lines represent one standard deviation from the mean. The results were obtained from 10 min mean vertical profiles from the 3rd until the 10th hour of the simulations.

of the boundary layer, around $z/h \sim 0.2$. The average height where $\overline{v'w'}$ crosses zero tends to decrease slightly in cases with higher surface heat flux. As shown in Figure 2e, this reflects the enhanced downward mixing of air with lower v due to stronger entrainment. The relatively large standard deviations indicate that during the averaging time period the wind and momentum fluxes are not in a stationary state. Additionally, the negative vertical gradients of V in the countergradient regime are small, approaching a vertically well-mixed state. Relatively small changes in the vertical profile of V in time can lead to relatively large changes in the height where V has its maximum value.

Having established that a countergradient regime for V is present in the specific case set up, most notably when the geostrophic wind vector is aligned with the $x-$axis, one may question whether these findings are perhaps only observed for this specific choice of coordinate system. To address this, we repeated the simulation with $\overline{w'\theta'}_{sfc} = 0.1$ mKs^{-1}, but with different angles of the geostrophic wind α_{geo} ranging from 10 to 90° in steps of 10°, with α_{geo} defined according to

$$\tan\alpha_{geo} \equiv \frac{V_g}{U_g}. \tag{14}$$

Another possibility to analyze the effect of α_{geo} on the countergradient regime is to rotate the LES wind fields, specifically those obtained for $\alpha_{geo} = 0$, by an angle α_{rot}. For $\alpha_{rot} = \alpha_{geo}$, the rotated LES wind field corresponds to a rotation of the geostrophic wind vector by the angle α_{geo}. The rotated horizontal wind can then be obtained from

$$\begin{aligned} u_{rot} &= u\cos\alpha_{rot} - v\sin\alpha_{rot}, \\ v_{rot} &= u\sin\alpha_{rot} + v\cos\alpha_{rot}. \end{aligned} \tag{15}$$

Similar to the reference runs, we diagnosed the lowest heights where V of the rotated wind field obtains its maximum value. We also diagnosed the lowest height where $\overline{v'w'}(z) < c_{crit}\overline{v'w'}_{sfc}$, with $c_{crit} = 0.01$. This choice is beneficial for obtaining a representative value for the height where $\overline{v'w'}$ is nearly zero, particularly since setting $c_{crit} = 0$ sometimes results in a height above the boundary layer, especially for cases with high values for α_{geo}.

Figure 5 compares V and $\overline{v'w'}$ obtained from the actual simulations with those based on the rotated fields, and finds that they are in close agreement. Additionally, the mean profiles of U for $\alpha_{geo} = 0$ and V for $\alpha_{geo} = 90°$ are almost identical (not shown). Due to the chaotic nature of turbulence, it is not expected that the results from the rotated wind fields and the actual simulations with a rotated geostrophic wind will be exactly identical.

From the horizontal lines shown in Figure 5, we can infer the dependence of the countergradient flux regime on α_{geo} and conclude that a countergradient regime is present for any value of α_{geo}. We note that for high values of α_{geo} ($\gtrsim$60°), the vertical gradient of V becomes very small in the countergradient regime.

In Section 4, we will use the vertical profiles of the mean wind and momentum fluxes to demonstrate that the eddy viscosities exhibit a strong directional dependence. We will also discuss how an anisotropic eddy viscosity controls the turning of the wind with height. Before doing so, we will first take a bulk perspective and, in the next subsection, discuss how the wind direction depends on the surface momentum fluxes and the boundary layer height, h.

3.3. The Impact of Surface Friction on the Wind Direction

To investigate the impact of the surface momentum fluxes on the turning of the wind, we performed two additional simulations, both with a surface heat flux of 0.01 mKs^{-1}, but with reduced surface roughness lengths of 0.01 and 0.001 m, respectively. Figure 6 shows that changes in the roughness length have little effect on the

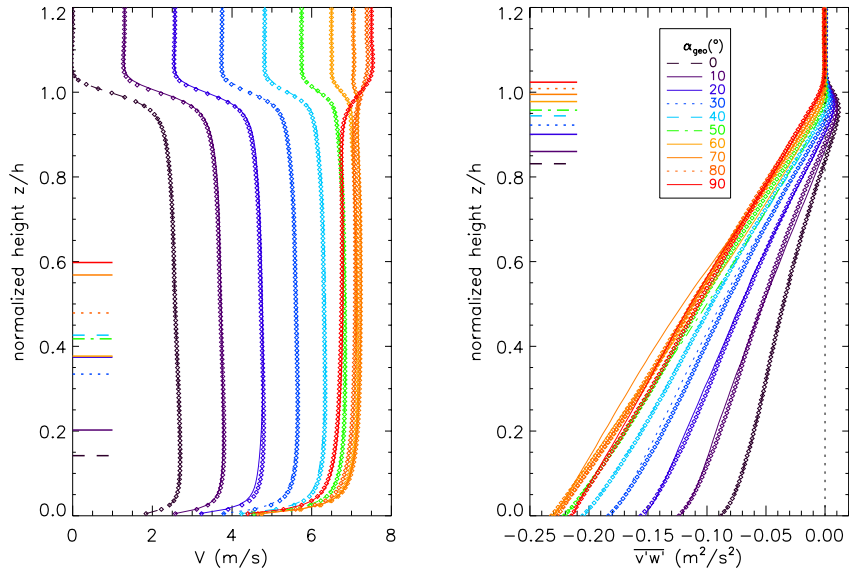

Figure 5. Vertical profiles of the hourly mean V and $\overline{v'w'}$ obtained during the 8th hour of the simulations, all with a prescribed surface heat flux of 0.1 mKs^{-1}. The solid lines indicate simulations with different directions of the geostrophic wind α_{geo}. The symbols denote results obtained by rotating the wind fields from the simulation with $\alpha_{geo} = 0$. The short horizontal lines show the heights of the maximum for V and where $\overline{v'w'} = 0$ in the actual simulations. The angles of the geostrophic wind are indicated in the legend.

growth of the convective boundary layer depth. However, a smoother ground surface leads to smaller momentum fluxes, an increase in U, a decrease in V, and a small increase in wind speed. The effect of surface friction is also clearly visible in the wind angle.

The impact of the surface momentum flux on the wind direction can be understood from the momentum budget equations. In case $V_g = 0$, applied as a large-scale forcing condition in our simulations, they can be written as

$$\begin{aligned} \frac{\partial U}{\partial t} &= fV - \frac{\partial \overline{u'w'}}{\partial z}, \\ \frac{\partial V}{\partial t} &= -f(U - U_g) - \frac{\partial \overline{v'w'}}{\partial z}. \end{aligned} \tag{16}$$

The values for the momentum fluxes at the surface can generally be expressed as,

$$\begin{aligned} \overline{u'w'}_{sfc} &= -C_d U_{spd,z_1} U_{z_1}, \\ \overline{v'w'}_{sfc} &= -C_d U_{spd,z_1} V_{z_1}, \end{aligned} \tag{17}$$

where the subscript "z_1" indicates a reference height above the ground, usually taken at 10 m, and C_d is a stability-dependent bulk drag coefficient which generally tends to increase for increasing surface roughness. The bulk effect of the surface fluxes on the wind can be quantified by approximating

$$-\frac{\partial \overline{u'w'}}{\partial z} \approx \frac{\overline{u'w'}_{sfc}}{h}, -\frac{\partial \overline{v'w'}}{\partial z} \approx \frac{\overline{v'w'}_{sfc}}{h}, \tag{18}$$

which indicates that a larger surface momentum flux exerts a stronger drag on the mean wind. Since the boundary layer depth for the three cases with different roughness length is nearly identical, we conclude that a rougher surface causes a stronger turning of the wind.

The turbulent eddies in the boundary layer transport low (high) horizontal momentum upward (downward) thereby influencing the wind direction. According to the momentum budget Equation 16, the positive slope of

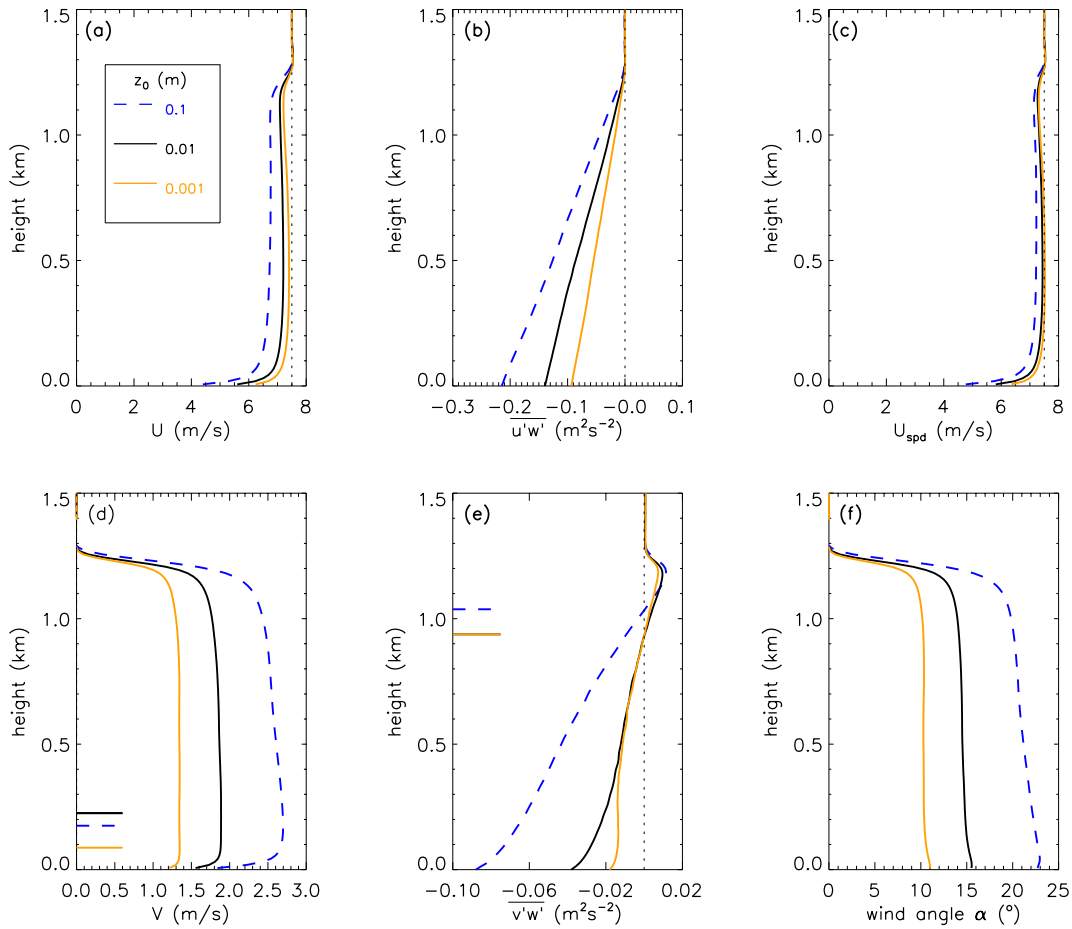

Figure 6. Vertical profiles of horizontal-slab averaged hourly-mean quantities similar to the ones shown in Figure 2, but now for different roughness length values according to the legend, and for simulations that were all forced by the same surface heat flux of 0.1 mKs^{-1}. The results were obtained during the 8th hour of the simulations.

$\overline{u'w'}$, originating from a minimum negative value near the surface, captures the damping effect of turbulence on U, as it causes U to become smaller than the geostrophic wind. This, in turn, tends to force V toward positive values since $-(U - U_g) > 0$. Following Equation 17 the positive values of V result in $\overline{v'w'}_{sfc}$ acquiring negative values. In fact, $\overline{v'w'}$ should increase with height, or similarly, $-\partial\overline{v'w'}/\partial z < 0$, to act as a sink (damping) term for V. If this condition were not satisfied, then under the condition $U < U_g$, V would tend to grow indefinitely.

Entrainment of momentum at the top of the boundary layer could also have been included, but given its relatively small contribution in the simulated cases considered here, it has been neglected in this analysis. We refer interested reader to De Roode and Siebesma (2020), who applied a conceptual mixed layer model to derive analytical solutions for the wind direction, including entrainment fluxes of momentum.

3.4. A Diagnosis of Eddy Viscosity Profiles

We will now show that the eddy viscosity profiles differ significantly between the two horizontal wind components. To this end we diagnosed the eddy viscosities from the mean horizontal winds and turbulent momentum fluxes according to,

$$\begin{aligned} \overline{u'w'} &= -K_{m,x}\frac{\partial U}{\partial z}, \\ \overline{v'w'} &= -K_{m,y}\frac{\partial V}{\partial z}. \end{aligned} \tag{19}$$

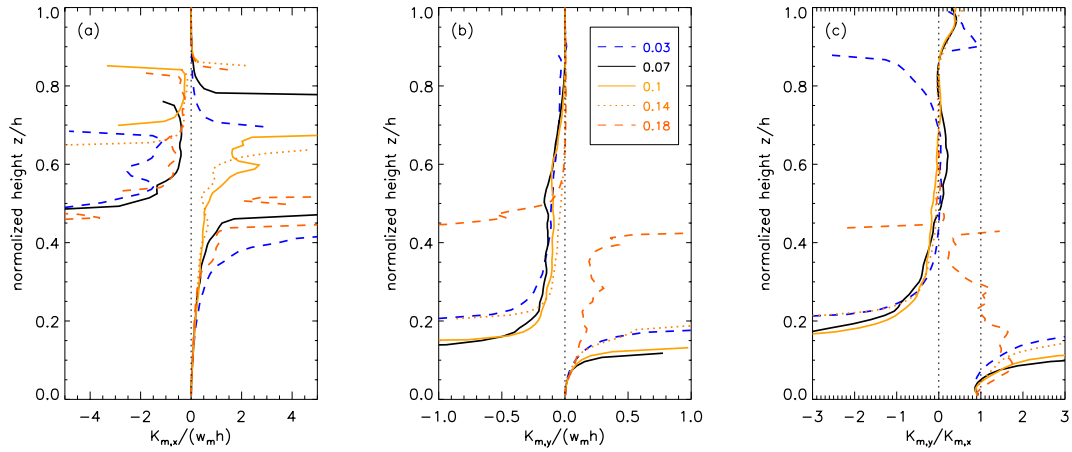

Figure 7. Diagnosed eddy viscosities for (a) the wind component parallel to the geostrophic wind, $K_{m,x}$, (b) the cross-isobaric wind component, $K_{m,y}$, both normalized by a factor $w_m h$, and (c) their ratio, $K_{m,y}/K_{m,x}$, during the 8th hour of the simulations. Surface heat flux values ($\overline{w'\theta'}_{sfc}$ in units of mKs^{-1}) are indicated in the legend. A ratio of unity, as indicated by one of the dotted vertical lines in (c), corresponds to the case where $K_{m,x}$ and $K_{m,y}$ are equal. The other dotted line in (c) indicates the zero line.

In this notation, $K_{m,x}$ and $K_{m,y}$ represent the eddy viscosities for the wind components in the zonal and meridional directions, respectively. These are used in parameterizations that assume vertical turbulent fluxes of horizontal momentum are directed down the mean vertical gradient of the wind. Figure 7 displays the eddy viscosities normalized by the boundary layer depth, h, and the scaling velocity, w_m, according to Equation 10. The normalized eddy viscosities $K_{m,x}$ for the horizontal wind component in the direction of the geostrophic wind ($\alpha_{geo} = 0°$), tend to obtain large values near the middle of the boundary layer. Additionally, the convective cases with wind shear can exhibit a countergradient flux regime for $\overline{u'w'}$ in the upper part of the boundary layer. In general, large values for the diagnosed eddy viscosities indicate vertically well-mixed profiles. If the vertical mean gradients of a quantity tend toward zero, the eddy viscosities will tend toward infinity to produce a non-zero momentum flux (see Equation 19). At this point, we conclude that the application of the normalization factor $w_m h$ does not yield an appropriate scaling behavior for $K_{m,x}$.

Figure 7b shows that the diagnosed eddy viscosity profiles, $K_{m,x}$ and $K_{m,y}$, are significantly different. In fact, $K_{m,y}$ exhibits negative values over a considerable depth in the interior of the boundary layer. As shown in Figure 3 this is a consequence of the vertical gradient of V and the momentum flux $\overline{v'w'}$ having the same sign. Approximating the small negative vertical gradients of V in the countergradient region as zero, which represents a perfectly vertically well mixed profile for V, would imply an eddy diffusivity $K_{m,y}$ tending toward infinity. In any case, the anisotropy factor, $K_{m,y}/K_{m,x}$, deviates strongly from unity, signifying a clear anisotropy in the eddy viscosities $K_{m,x}$ and $K_{m,y}$.

4. Momentum Flux Budgets

To address the question why the cross-isobaric momentum flux can become countergradient, it is instructive to analyze the momentum flux budget (Dixit et al., 2021; Larson et al., 2019). For horizontally homogeneous conditions, which are naturally satisfied in the LESs due to the horizontally periodic boundary conditions, the budget equations for the resolved momentum fluxes can be derived from the filtered budget momentum equations (see Stull (1988) for details),

$$\underbrace{\frac{\partial \overline{u'w'}}{\partial t}}_{\text{tendency}} = \underbrace{-\overline{w'w'}\frac{\partial U}{\partial z}}_{\text{shear}} + \underbrace{f\overline{v'w'}}_{\text{Coriolis}} - \underbrace{\frac{\partial \overline{w'w'u'}}{\partial z}}_{\text{turbulent transport}} + \underbrace{\beta \overline{u'\theta'_v}}_{\text{buoyancy}} - \underbrace{\overline{u'\frac{\partial \pi'}{\partial z}}}_{P_1} - \underbrace{\overline{w'\frac{\partial \pi'}{\partial x}}}_{P_2} - \underbrace{\overline{w'\frac{\partial \tau'_{1j}}{\partial x_j}} - \overline{u'\frac{\partial \tau'_{3j}}{\partial x_j}}}_{\text{subgrid}}, \tag{20}$$

$$\frac{\partial \overline{v'w'}}{\partial t} = \underbrace{-\overline{w'w'}\frac{\partial V}{\partial z}}_{P_1} \underbrace{-f\overline{u'w'}}_{C} \underbrace{-\frac{\partial \overline{w'w'v'}}{\partial z}}_{T} + \underbrace{\beta\overline{v'\theta_v'}}_{B} \underbrace{-\overline{v'\frac{\partial \pi'}{\partial z}}}_{P_2} \underbrace{-\overline{w'\frac{\partial \pi'}{\partial y}}}_{P_2} \underbrace{-\overline{w'\frac{\partial \tau_{2j}'}{\partial x_j}}}_{\text{subgrid}} \underbrace{-\overline{v'\frac{\partial \tau_{3j}'}{\partial x_j}}}_{\text{subgrid}}. \quad (21)$$

The names of the terms in the momentum flux budget Equation 21, as used in the subsequent discussion, are indicated with underbraces. Except for terms denoted by "subgrid", all terms were computed from the resolved fields. The pressure terms P_1 and P_2 are sometimes expressed differently, for example, with a term that includes spatial derivatives of pressure fluxes (Heinze et al., 2015). However, the different forms of the pressure terms are mathematically equivalent and can be derived with straightforward manipulation involving the mass conservation equation (Stull, 1988). We diagnosed all the budget terms except for the one involving the fluctuations of the subgrid momentum flux τ_{ij}. Diagnosing the fluctuating part of the subgrid stress term is challenging because according to Equation 6 τ_{ij} depends on both the subgrid TKE and spatial gradients of the wind. Moreover, τ_{ij} represents the subgrid momentum flux, which, away from the surface, is significantly smaller than the resolved momentum flux suggesting that it is likely to be a less important term. In addition, the kappa advection scheme introduces some numerical diffusion, further contributing to the effective diffusion in a manner similar to the subgrid term in the momentum flux budget equation.

In the subsequent discussion, we use the term "production" when a term in the momentum budget contributes to a tendency with the same sign as the momentum flux itself. We will restrict our analysis to a qualitative examination of the momentum flux budgets. We begin by examining the budget for $\overline{u'w'}$ as presented in Figure 8. The predominantly negative values for $\overline{u'w'}$, as shown in Figure 2b, are produced by the shear term.

In the lower parts of the convective boundary layers, the buoyancy term $\beta\overline{u'\theta_v'}$ also contributes to negative tendencies for $\overline{u'w'}$. The heat flux is positive up to $z/h \sim 0.7$ (see Figure 1b), which indicates that updrafts are, on average, positively buoyant. To illustrate this, we applied conditional sampling to obtain the mean updraft values (indicated with a subscript "up") for U_{up}, V_{up}, Θ_{up}, W_{up}, and the area updraft fraction σ. Details of the sampling operator are explained in De Roode and Bretherton (2003).

As shown in Figure 9, the negative values of $\overline{u'\theta_v'}$ indicate that the rising, warm, positively buoyant plumes ($W_{\text{up}} > 0, \Theta_{\text{up}} - \Theta > 0$), have, on average, a smaller horizontal velocity than the slab-mean value ($U_{\text{up}} - U < 0$). This can be explained by the fact that the rising air originates from the surface layer, where the wind speed is generally low, due to the no-slip condition at the ground. The downdrafts transport relatively high horizontal velocities from the top of the boundary layer, where the wind is close to the geostrophic value.

For all cases the presence of a maximum in V leads to a change in the sign of the shear term in the $\overline{v'w'}$ budget. The buoyancy term, $\beta\overline{v'\theta_v'}$, contributes to the production of negative $\overline{v'w'}$ values well above the height where V reaches its maximum value. The sign of $\beta\overline{v'\theta_v'}$ can also be explained from Figure 9, which shows that positively buoyant plumes transport low V_{up} values from the surface upward.

The turbulent transport term is a redistribution term in the sense that its vertical integral is zero. For all cases $-\partial_z\overline{w'w'u'}$ is positive in the lower part of the boundary layer, thereby opposing the negative values of $\overline{u'w'}$, whereas in the upper part it acts to produce negative $\overline{u'w'}$. The turbulent transport $-\partial_z\overline{w'w'v'}$ is negative in the middle part of the boundary layer thereby supporting the negative, countergradient flux values for $\overline{v'w'}$.

The P_1 pressure terms in the budgets of both $\overline{u'w'}$ and $\overline{v'w'}$, $-\overline{u'\partial\pi'/\partial z}$ and $-\overline{v'\partial\pi'/\partial z}$, respectively, have qualitatively similar vertical profiles. Both pressure terms are predominantly positive meaning that they act to oppose the negative signs of $\overline{u'w'}$ and $\overline{v'w'}$. Near the top of the boundary layer, the P_1 pressure terms tend to counteract the buoyancy terms, which are particularly large in this region. This is likely due to plumes rising into the relatively warm inversion layer, generating significant fluctuations in θ.

The P_2 pressure term $-\overline{w'\partial\pi'/\partial x}$ is positive in the $\overline{u'w'}$ budget, while $-\overline{w'\partial\pi'/\partial y}$ is negative in the $\overline{v'w'}$ budget. The P_2 terms include horizontal pressure gradients that drive horizontal wind fluctuations. These horizontal

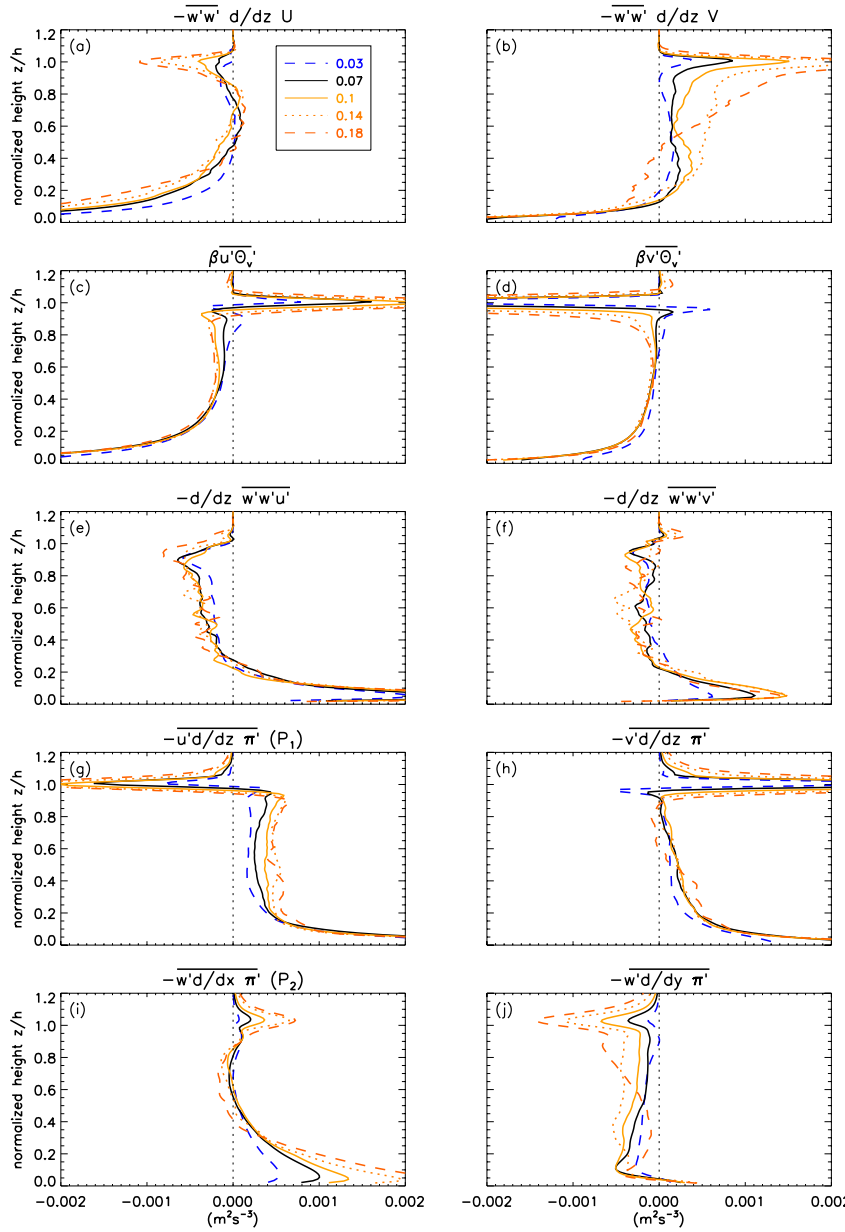

Figure 8. Budgets for the resolved momentum flux $\overline{u'w'}$ and $\overline{v'w'}$ with the titles of the subplots representing the terms present in Equations 20 and 21 (subplots a, c, e, g, i and b, d, f, h, j, respectively). The results represent an hourly-mean value as obtained during the 8th hr of the simulations. The vertical dotted line represents the zero value. The linestyles are according to the legend in panel (a).

pressure gradients are sufficiently different to establish a mean correlation with the vertical velocity that vary in sign between the $\overline{u'w'}$ and $\overline{v'w'}$ momentum budgets.

In conclusion, for convective cases with wind shear the countergradient flux of the cross-isobaric wind component is promoted by the buoyancy and transport terms, as well as by fluctuations in the horizontal pressure gradients.

5. The Impact of Anisotropic Eddy Viscosities on the Ekman Wind Profile

We will now refine our analysis of the turning of the wind by exploring the consequences of anisotropic eddy viscosities on the vertical profile of the horizontal wind. To do this, we will revisit the Ekman spiral model, whose

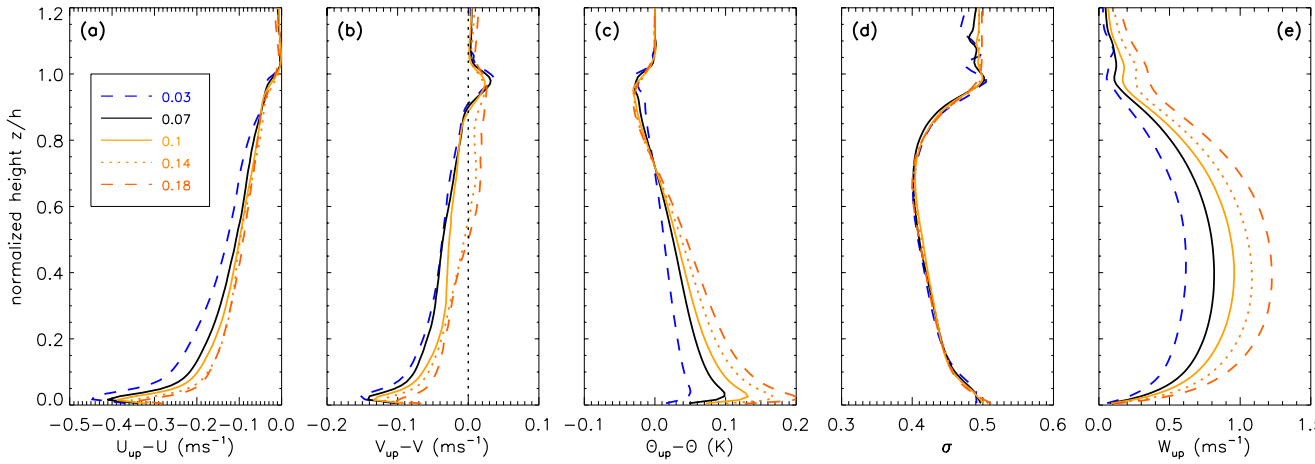

Figure 9. Vertical profiles of the difference between the mean values in updrafts and the horizontal slab mean values, (a) $U_{up} - U$, (b) $V_{up} - V$ and (c) $\Theta_{up} - \Theta$, (d) the updraft area fraction σ, and (e) the mean vertical velocity in the updrafts W_{up}. The results were obtained during the 8th hour of the simulations. The legend indicates the values of the surface heat flux in units of mKs^{-1}.

solution is derived from the steady-state momentum budget equations assuming a constant eddy viscosity. It is important to note that we neither advocate the use of a downgradient diffusion approach, as it would contradict the findings of countergradient momentum transport, nor the application of anisotropic eddy viscosity. At this point, however, we are solely interested in exploring the potential consequences of applying an anisotropic eddy viscosity. To the best of our knowledge, this type of analysis has not been made before. Since widely used models, such as the ECWMF, employ the traditional downgradient diffusion approach for turbulent momentum fluxes (ECMWF, 2023), we believe that the following analysis provides valuable insight into the understanding of such turbulence closure techniques, in particular for shear-driven convective boundary layers with anisotropic eddy viscosities such as found from the LES results.

5.1. A Modified Analytical Solution for the Ekman Wind Spiral

We will use the momentum budget Equation 16, which implicitly assume a coordinate system with the x-axis aligned with the geostrophic wind, following $U_g > 0$, and $V_g = 0$. We assume U_g to be constant with height. Anisotropic diffusion is incorporated by applying the momentum flux parameterizations from Equation 19, where $K_{m,y} = cK_{m,x}$, with c representing an anisotropy factor for the eddy viscosities in the two horizontal directions. To facilitate analytical solutions, we will use eddy viscosities that are constant with height. With this framework, the steady-state momentum budget equations can be expressed as

$$\begin{aligned} 0 &= fV + K_{m,x}\frac{\partial^2 U}{\partial z^2}, \\ 0 &= -f(U - U_g) + K_{m,y}\frac{\partial^2 V}{\partial z^2}. \end{aligned} \tag{22}$$

The use of constant eddy viscosities allows us to express the second derivatives with respect to height in the above equations,

$$\frac{\partial^2 V}{\partial z^2} = -\frac{K_{m,x}}{f}\frac{\partial^4 U}{\partial z^4} \tag{23}$$

$$\frac{\partial^2 U}{\partial z^2} = \frac{K_{m,y}}{f}\frac{\partial^4 V}{\partial z^4}. \tag{24}$$

We can substitute the latter two back in Equation 22 to obtain

$$\frac{\partial^4 V}{\partial z^4} + \frac{f^2}{K_{m,x} K_{m,y}} V = 0$$
$$\frac{\partial^4 U}{\partial z^4} + \frac{f^2}{K_{m,x} K_{m,y}} (U - U_g) = 0 \tag{25}$$

For the given boundary conditions of no-slip at the ground surface, $U = V = 0$ at $z = 0$, and $U \to U_g$, $V \to V_g = 0$ for $z \to \infty$, the solutions become

$$U = U_g (1 - e^{-\gamma z} \cos \gamma z),$$
$$V = \frac{1}{\sqrt{c}} U_g e^{-\gamma z} \sin \gamma z. \tag{26}$$

Here, γ is defined as

$$\gamma \equiv \sqrt[4]{\frac{f^2}{4 K_{m,x} K_{m,y}}} = \frac{1}{c^{1/4}} \sqrt{\frac{f}{2 K_{m,x}}} \tag{27}$$

We recall that for $c = 1$, we have $K_{m,x} = K_{m,y} = K_m$, with which we obtain the original Ekman wind solution as shown in Figure 10. The figure also shows solutions for an anisotropic eddy diffusivity with $c = 0.5$ which will be discussed next.

5.2. Interpretation of the Modified Ekman Wind Spiral

The presence of the prefactor $1/\sqrt{c}$ in the solution for V follows from a substitution of the general solutions in the momentum budget Equation 22. The inclusion of the factor c has an important consequence for the turning of the wind, whose solution is given by

$$\alpha \equiv \arctan \frac{V}{U} = \arctan \left(\frac{1}{\sqrt{c}} \frac{e^{-\gamma z} \sin \gamma z}{1 - e^{-\gamma z} \cos \gamma z} \right). \tag{28}$$

Therefore, we conclude that for any $c \neq 1$, or, in other words, $K_{m,x} \neq K_{m,y}$, the wind angle will deviate from the original Ekman spiral solution.

With use of the downgradient momentum flux expressions Equation 19, the analytical solutions for the momentum fluxes can be written as

$$\overline{u'w'} = -U_g K_{m,x} \gamma e^{-\gamma z} (\cos \gamma z + \sin \gamma z),$$
$$\overline{v'w'} = -U_g \sqrt{c} K_{m,x} \gamma e^{-\gamma z} (\cos \gamma z - \sin \gamma z). \tag{29}$$

With aid of this solution we find the following momentum flux values at the ground surface,

$$\overline{u'w'}_{sfc} = -\frac{U_g}{c^{1/4}} \sqrt{\frac{f K_{m,x}}{2}},$$
$$\overline{v'w'}_{sfc} = -U_g c^{1/4} \sqrt{\frac{f K_{m,x}}{2}}, \tag{30}$$

and consequently the surface friction velocity becomes

$$u_* = \sqrt{U_g} \left(\frac{f K_{m,x}}{2} \right)^{1/4} \left(\frac{1}{\sqrt{c}} + \sqrt{c} \right)^{1/4} \tag{31}$$

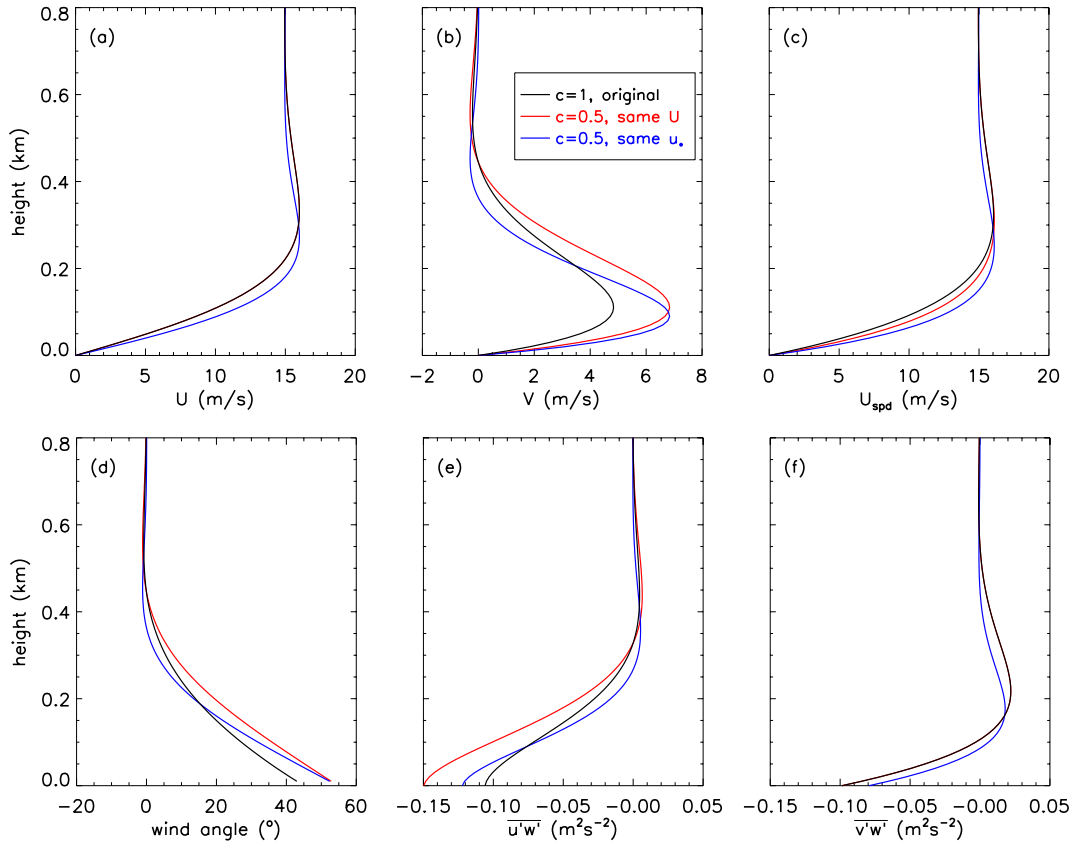

Figure 10. Three analytical solutions for the Ekman spiral are depicted, featuring vertical profiles for (a) U, (b) V, (c) U_{spd}, (d) the wind direction, and the momentum fluxes (e) $\overline{u'w'}$ and (f) $\overline{v'w'}$. The black line represents the original Ekman spiral for $K_{\text{m}} = 1\ \text{m}^2\text{s}^{-1}$. The red line is obtained for $K_{\text{m},y}/\sqrt{c} = \sqrt{c}K_{\text{m},x} = 1\ \text{m}^2\text{s}^{-1}$, with $c = 0.5$. For any value of c, the solutions for U and $\overline{v'w'}$ are identical to the original Ekman spiral solution. The blue line indicates solutions for $c = 0.5$ and $K_{\text{m},y} = cK_{\text{m},x}$, with $K_{\text{m},y}$ chosen such that the surface friction velocity according to Equation 31 is identical to the original Ekman spiral solution shown by the black line.

Figure 10 compares the solutions of the Ekman spiral for $c = 0.5$ and 1. For the case with an anisotropic eddy diffusivity ($c = 0.5$) we requested the same value for γ as for $c = 1$, which according to Equation 27 is obtained for $K_{\text{m},x}K_{\text{m},y} = K_m^2$, and consequently we used $K_{\text{m},y} = cK_{\text{m},x} = \sqrt{c}K_m$. For this specific choice, the vertical profiles for U and $\overline{v'w'}$ are invariant to changes in c. For a reduction of c down to a value of 0.5, V is increased with respect to the original solution $c = 1$. This result underscores the main point of the present study: the application of anisotropic eddy viscosities introduces an additional controlling factor on the turning of the wind. Notably, for the same profile for U, the analytical results demonstrate a stronger turning of the wind when $K_{\text{m},y} < K_{\text{m},x}$.

However, a careful inspection reveals that the modified case exhibits more negative momentum fluxes $\overline{u'w'}$. One could argue that this is a scenario with different boundary conditions at the ground surface than the original Ekman wind solution. To address this concern, we present a third case which, like the second case, also applies $c = 0.5$ and uses $K_{\text{m},y} = cK_{\text{m},x}$. However, eddy viscosities are adjusted to obtain the same value for u_* as in the original Ekman spiral case ($c = 1$ and $K_{\text{m}} = 1\ \text{m}^2\text{s}^{-1}$). This adjustment could be achieved straightforwardly with the help of Equation 31, which gives,

$$K_{\text{m},y} = 2K_{\text{m}}\left(\frac{1}{c^{3/2}} + \frac{1}{c^{1/2}}\right)^{-1}. \tag{32}$$

For this setting, we find that particularly in the lower half of the boundary layer, the wind angle increases compared to the original Ekman spiral solution.

Let us investigate the influence of eddy diffusivity magnitude on the mean vertical profile of any arbitrary quantity φ. The surface flux $\overline{w'\varphi'}_{\mathrm{sfc}}$ is typically determined from a parameterization, for example, such as one based on Monin-Obukhov similarity theory. With use of the eddy diffusivity approach (Equation 1), if follows that the mean vertical gradient of $\overline{\varphi}$ must satisfy the following relation,

$$\frac{\partial \overline{\varphi}}{\partial z} = -\frac{\overline{w'\varphi'}}{K_{\varphi}}. \tag{33}$$

This expression indicates that the same flux profile could be obtained with a vertical mean profile of $\overline{\varphi}$ that has adapted itself to the applied eddy diffusivity profile. In other words, if K_{φ} were reduced, larger values for the vertical gradient of $\overline{\varphi}$ could give the same flux profile. This is precisely what we have found with the modified Ekman spiral solution labeled as "c = 0.5, same U" in Figure 10. For the same vertical profile of $\overline{v'w'}$, a reduced value for $K_{\mathrm{m},y}$ leads to larger vertical gradients for V and, consequently, a stronger turning of the wind with height.

5.3. Analogies With the Bulk Anisotropic Rayleigh Friction Model

The modified anisotropic Ekman model has demonstrated that an anisotropic diffusion approach has a distinct impact on the wind profile. Here we will argue that this finding has some commonality with studies by Deser (1993) and Stevens et al. (2002), who both applied a bulk steady-state Anisotropic Rayleigh Friction Model,

$$\begin{aligned} 0 &= f(V_{\mathrm{bl}} - V_{\mathrm{g}}) - \epsilon_x U_{\mathrm{bl}} \\ 0 &= -f(U_{\mathrm{bl}} - U_{\mathrm{g}}) - \epsilon_y V_{\mathrm{bl}} \end{aligned} \tag{34}$$

with the subscript "bl" denoting the mean value of the wind in the turbulent atmospheric boundary layer. The factors ϵ_x and ϵ_y are anisotropic bulk Rayleigh friction factors that can differ from one another. They represent the bulk friction effect due to the turbulent momentum fluxes, for example, like

$$\epsilon_x U_{\mathrm{bl}} = \frac{\partial \overline{u'w'}}{\partial z} \approx \frac{\overline{u'w'}_h - \overline{u'w'}_{\mathrm{sfc}}}{h}, \tag{35}$$

with the subscript h denoting the value of the flux at the top of the boundary layer. With aid of the surface flux parameterization Equation 17 and the flux-jump relation Equation 13 we can write,

$$\epsilon_x U_{\mathrm{bl}} = \frac{C_{\mathrm{d}} U_{\mathrm{spd}_{\mathrm{bl}}} U_{\mathrm{bl}} - w_{\mathrm{e}}\left(U_{\mathrm{ft}} - U_{\mathrm{bl}}\right)}{h} \tag{36}$$

where we used the fact that in a bulk model approach the boundary-layer wind is constant with height. The subscript "ft" denotes the value of the wind just above the boundary layer. With this model Deser (1993) was able to represent the observed winds over the tropical Pacific, but only if she allowed $\epsilon_x \neq \epsilon_y$. Stevens et al. (2002) explained that the application of an anisotropic bulk friction factor is due to the different entrainment fluxes for the zonal and meridional wind components.

We will now use the analytical modified Ekman spiral solutions to show that the bulk friction factors ϵ_{x} and ϵ_{y} are different. Since the analytical solutions were obtained with the $x-$axis in the direction of the geostrophic wind, ϵ_{x} represents the bulk friction factor in the direction of the geostrophic wind. We are particularly interested in the question as to how the asymmetry factor $c = K_{\mathrm{m},y}/K_{\mathrm{m},x}$ affects these two bulk friction factors. From an integration of the stationary momentum equations Equation 34 up to the top of the boundary layer we can diagnose the bulk friction factors according to

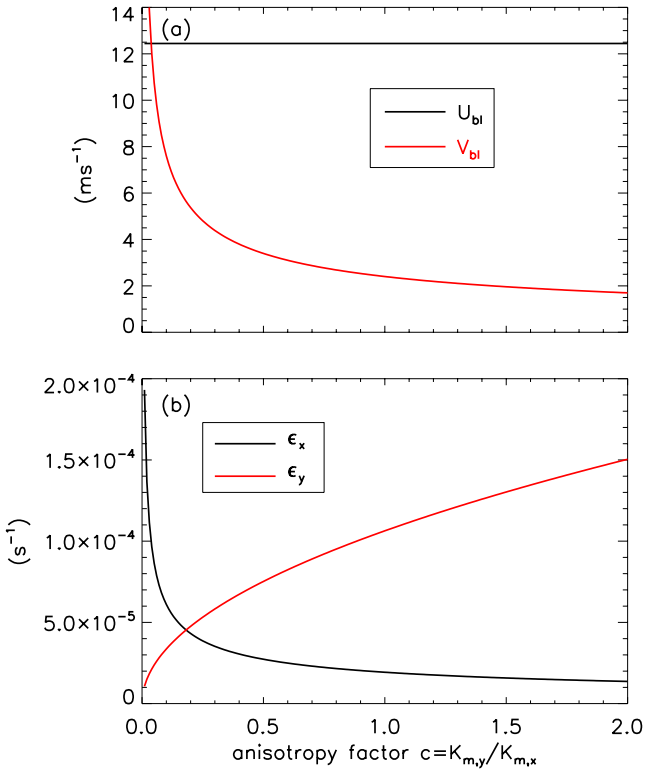

Figure 11. (a) The mean values of wind in the boundary layer and (b) the values of the bulk friction factors. The results were diagnosed from the modified Ekman spiral solution.

$$\epsilon_x = f\frac{\int_0^h V dz'}{\int_0^h U dz'}$$
$$\epsilon_y = -f\frac{\int_0^h (U-U_g)\,dz'}{\int_0^h V dz'} \tag{37}$$

Figure 11a shows the mean boundary layer wind velocities that were found from an integration of the analytical modified Ekman spiral solutions up to a height $\gamma z = \pi$ at which $e^{-\gamma z} = 0.0432$. It shows that U does not depend on the factor c, whereas V tends to decrease with increasing c. These solutions were used, in turn, to diagnose the bulk friction coefficients as shown in Figure 11b. It is interesting to note that for an isotropic eddy viscosity ($c = 1$) $\epsilon_x \neq \epsilon_y$. In other words, if a bulk model would be used to represent the mean wind as obtained from the original Ekman model anisotropic bulk friction factors would be needed. Last, we would like to mention an analytical solution for the bulk friction factor for the cross-isobaric wind component, which follows straightforwardly from the analytical solution for the modified Ekman spiral for the limit $h \to \infty$,

$$\epsilon_y = \sqrt{c} f. \tag{38}$$

Interestingly, for isotropic diffusion, $c = 1$, we find that the bulk friction coefficient for the cross-isobaric component of the mean wind is equal to the Coriolis parameter f. By contrast, for anisotropic diffusion, $c \neq 1$, we find that the bulk friction coefficient ϵ_y changes proportionally to $\sqrt{c}$.

6. Discussion

We have found that for clear convective boundary layers with wind shear the LES results do not support the use of a uniform eddy viscosity profile for both horizontal wind components. When both $\overline{v'w'}$ and the vertical gradient of V have the same sign, a downgradient momentum flux parameterization with positive eddy viscosity would incorrectly predict the sign of $\overline{v'w'}$. Moreover, if the small negative vertical gradients of V in the countergradient regime would be neglected, for instance, by approximating $\partial V/\partial z = 0$, a downgradient diffusion approach would yield an erroneous zero momentum flux. In this section we will briefly discuss two possible parameterization approaches to overcome this situation. One is based on a higher-order closure model (André et al., 1978), and the other combines an eddy diffusivity approach with a massflux contribution to the flux (Siebesma et al., 2007). Furthermore, we will address an important consequence of countergradient momentum transport on the exchange of kinetic energy between the mean flow and the turbulent field.

6.1. Higher-Order Closure Models

Larson et al. (2019) found countergradient momentum transport in shallow cumulus cloud fields. For example, their study proposed to parameterize the countergradient transport for $\overline{v'w'}$ as follows,

$$\overline{v'w'} = -\frac{\tau_{turb}\overline{w'^2}}{C_6}\frac{\partial V}{\partial z} + \frac{\tau_{turb}}{C_6}(1-C_7)\beta\overline{v'\theta_v'} - \frac{\tau_{turb}}{C_6}\frac{1}{\overline{\rho}}\frac{\overline{\rho}\overline{w'w'v'}}{\partial z}, \tag{39}$$

with C_6 and C_7 proportionality factors, the higher-order moments $\overline{w'^2}$, $\overline{v'\theta_v'}$ and $\overline{w'w'v'}$ are unknown quantities that need to be determined. The pressure terms present in the momentum budget equation are absorbed into the time scale τ_{turb} and the factor C_6. The first term on the right-hand-side can be interpreted as a downgradient diffusion term, with an eddy viscosity K_m that depends on the intensity of the vertical velocity fluctuations, as quantified by its variance, and a turbulent time scale τ_{turb} (Larson et al., 2019),

$$K_{\mathrm{m}} = \frac{\tau_{\mathrm{turb}}\overline{w'^2}}{C_6}. \tag{40}$$

Note that this factor K_{m} is commonly present in the parameterizations for $\overline{u'w'}$ and $\overline{v'w'}$ (Bougeault, 1981). In analogy with molecular diffusion, it is also positive definite. Following Equation 39, any countergradient momentum transport should therefore be produced by the terms containing $\overline{v'\theta'_{\mathrm{v}}}$ and $\overline{w'w'v'}$. We find that this is consistent with the buoyancy and turbulent transport terms for the cases shown in Figures 8d and 8f. Both $\overline{v'\theta'_{\mathrm{v}}}$ and the pressure term $-\overline{w'\partial_y\pi'}$ contribute to a negative value for $\overline{v'w'}$, although this effect is somewhat counteracted by the pressure term $-\overline{v'\partial_z\pi'}$.

6.2. Eddy Diffusivity With Massflux Approach

Another option for allowing countergradient momentum transport is to include a massflux contribution in the parameterized momentum flux, according to (De Rooy et al., 2022; Siebesma et al., 2007; Teixeira et al., 2023),

$$\overline{w'\varphi'} = -K_{\mathrm{h}}\frac{\partial\overline{\varphi}}{\partial z} + \sigma w_{\mathrm{up}}\left(\varphi_{\mathrm{up}} - \varphi_{\mathrm{down}}\right). \tag{41}$$

This parameterization requires determining the area fraction of updrafts, σ, and the mean values of φ in both updrafts and downdrafts, as indicated by the subscripts "up" and "down," respectively. Note that the downdraft component can be straightforwardly obtained from the following definition (Randall et al., 1992),

$$\overline{\varphi} = \sigma\varphi_{\mathrm{up}} + (1-\sigma)\varphi_{\mathrm{down}}, \tag{42}$$

or equivalently,

$$\varphi_{\mathrm{up}} - \varphi_{\mathrm{down}} = \frac{\varphi_{\mathrm{up}} - \overline{\varphi}}{1-\sigma}. \tag{43}$$

For small σ it follows that $\varphi_{\mathrm{down}} \approx \overline{\varphi}$. The EDMF approach is applied in the ECMWF global weather forecast model to represent convective transport in the atmosphere (ECMWF, 2023), except for the momentum flux in the clear convective boundary layer. The results presented in Figure 9b suggest that the inclusion of a massflux term could aid to produce a countergradient momentum flux, in particular in the lower part of the clear convective boundary layer where $V_{\mathrm{up}} - V < 0$. The inclusion of a mass-flux contribution to the momentum flux could possibly improve the model representation of wind, but this may require a careful reconsideration of the associated eddy diffusivity profile to ensure consistency between local and non-local mixing contributions in momentum transport.

To apply the EDMF approach to momentum requires an extra equation to predict the updraft velocities U_{up} and V_{up}. This involves a horizontal mixing term that captures the entrainment and detrainment of horizontal momentum between the updrafts and the downdrafts, but also a pressure term (Lappen & Randall, 2006).

6.3. Kinetic Energy Transfer

The presence of countergradient momentum transport therefore has an important implication on the production of horizontal velocity fluctuations. For example, the shear production of $\overline{v'v'}$ is given by,

$$\left(\frac{\partial\overline{v'v'}}{\partial t}\right)_{\mathrm{prod}} = -2\overline{v'w'}\frac{\partial V}{\partial z}. \tag{44}$$

If the flux $\overline{v'w'}$ is counter to the mean gradient, the production term becomes negative and will actually act to dissipate variance $\overline{v'v'}$.

The production term in Equation 44 also appears in the mean kinetic energy equation, but with opposite sign. This can be derived from the momentum budget Equation 16. If we only consider the turbulent flux term on the rhs of the budget equation for V, and multiply it by V, we get

$$\begin{aligned}\frac{\partial V^2}{\partial t} &= -2V\frac{\partial \overline{v'w'}}{\partial z} \\ &= -2\frac{\partial V\overline{v'w'}}{\partial z} + 2\overline{v'w'}\frac{\partial V}{\partial z},\end{aligned} \tag{45}$$

where we applied the chain rule of differentiation. The first term on the rhs is a redistribution term of kinetic energy. This can be understood from its vertical integration from the ground surface, where $V = 0$, to just above the top of the turbulent boundary layer, where $\overline{v'w'} = 0$. These boundary conditions give a zero value for the vertical integral. In case of a countergradient momentum flux, the second term will be positive, indicating that the kinetic energy that is lost from the turbulent fluctuations $\left(\overline{v'v'}\right)$, is gained by the mean flow $\left(V^2\right)$. In other words, under countergradient momentum flux conditions there will be an upscale transport of energy from the small-scale turbulent fluctuations to the mean flow.

7. Conclusions and Recommendations

This paper analyzes results from LESs to demonstrate the presence of a distinct countergradient momentum flux regime in dry convective boundary layers with wind shear. The simulations were forced by a constant horizontal pressure gradient, driving a geostrophic wind U_g of 7.5 ms^{-1} in the $x-$direction, and $V_g = 0$ in the $y-$direction. The cases were forced by different surface heat fluxes in the range between 0.03 and 0.18 mKs^{-1}.

In the bulk part of the convective boundary layers, we find that the mean vertical gradient of the cross-isobaric wind V can have the same sign as its flux $\overline{v'w'}$, signifying countergradient momentum transport. Although less pronounced, this is also found for the wind component in the direction of the geostrophic wind U in the upper part of the boundary layer. The countergradient momentum flux $\overline{v'w'}$ can be explained by the boundary conditions, which dictate zero values for V at the ground surface due to the no-slip condition, and just above the boundary layer because of $V_g = 0$. The maximum value for V is found in the lower part of the boundary layer, while the momentum flux $\overline{v'w'}$ remains negative from the ground surface to near the top of the boundary layer. Between the heights where V peaks and where the $\overline{v'w'}$ changes sign, the vertical gradient of V and $\overline{v'w'}$ have the same sign. This kind of countergradient momentum transport has also been reported in fields of shallow cumulus by Larson et al. (2019), Helfer et al. (2021) and Dixit et al. (2021). We also find from additional simulations that a countergradient momentum flux regime is present for any arbitrary angle of the geostrophic wind.

Buoyant updrafts play a crucial role in driving countergradient momentum fluxes. They are capable of vertically transporting air with relatively small horizontal momentum, originating from near the surface, to much higher altitudes within the boundary layer compared to conditions without a buoyancy flux, such as in the neutral boundary layer. The upward transport of low horizontal momentum promotes a negative momentum flux. If the momentum flux $\overline{v'w'}$ remains negative above the height where V reaches its maximum, the momentum flux becomes countergradient. This type of boundary-layer scale transport can be interpreted as non-local transport, similar to the countergradient transport for heat found in the clear convective boundary layer (Holtslag & Moeng, 1991).

The LES fields also allow for the diagnosis of eddy viscosity profiles, which are found to be anisotropic, meaning that they differ for the two horizontal wind components. In fact, the presence of countergradient momentum fluxes implies that their parameterization with a downgradient diffusion approach would require negative eddy viscosity values. We have explored the impact of anisotropic eddy viscosity profiles through the theoretical Ekman spiral equations. If we relax the assumption of a uniform, constant eddy viscosity and allowing the eddy viscosities for U and V to differ by a constant factor, that is $K_{m,y} = cK_{m,x}$, we find that this leads to modifications in the turning of the wind with height. In this context it is interesting to mention that De Roode (2007) reported that in a marine stratocumulus boundary layer eddy diffusivity profiles for heat and moisture can be different, too.

The use of a negative eddy viscosity can be avoided by employing parameterizations that allow for non-local transport. Such schemes can be derived from the momentum budget equation (Larson et al., 2019) or by following an eddy-diffusivity with massflux approach (Siebesma et al., 2007). The optimization of parameterization constants, time scales, or lateral entrainment in these schemes can be fine-tuned using LES results. By rotating the LES fields, it is possible to investigate how these factors depend on the direction of the geostrophic wind.

The mechanical shear production of turbulent wind fluctuations becomes negative when the momentum flux is countergradient. The impact of this on the spatial organization of convective structures is an interesting question (Park et al., 2018; Salesky et al., 2017), particularly from the perspective of weather forecast models that operate with mesh sizes at kilometer-scale resolutions (De Roode et al., 2019). Traditionally, weather forecast and climate models implicitly assume that all turbulent vertical transport occurs at unresolved subgrid scales. However, as the resolution becomes fine enough, this assumption no longer holds, and some fraction of the turbulent transport will be resolved. This situation necessitates modifications of subgrid parameterizations for turbulent transport by making them scale-aware (Honnert et al., 2011).

The turning of the wind matters for large-scale dynamics, particularly since it controls the large-scale vertical motions in the atmosphere, such as the large-scale subsidence in a high-pressure system (De Roode & Siebesma, 2020). The same holds for the vertical motions in the global oceans, often referred to as Ekman pumping or sinking. This makes the present study also relevant for the modeling of such flow in global ocean models, mainly because the vertical fluxes of heat and momentum are often computed with an eddy diffusion approach, similar to large-scale atmospheric models.

Data Availability Statement

The DALES model is publicly available from https://github.com/dalesteam/dales which includes instructions to compile and execute the model. It is also archived on Zenodo (Arabas et al., 2024). We have posted the results at www.euclipse.nl/Countergradient/countergradient.tar, which includes the input files (prof.inp, lscale.inp, namoptions) for each case reported in this study. With the use of these input files all the results discussed in the study can be duplicated on any arbitrary computer platform.

Acknowledgments
Stephan de Roode acknowledges funding from the NWO sponsored research project "Renewable Energy Forecasts from Observations and high-Resolution Modeling" (REFORM) with project number 18657 of the research programme Open Technology which is financed by the Dutch Research Council (NWO), Greenchoice and Whiffle. We would like to thank the Dutch Olympic sailor Annette Duetz who sparked the present research with her BSc research project on the organization of wind streaks in the stable atmospheric boundary layer. Last, we wish to express our gratitude to two anonymous reviewers for their critical yet constructive suggestions that have helped to improve the original version of this manuscript.

References

André, J., De Moor, G., Lacarrere, P., & Du Vachat, R. (1978). Modeling the 24-hour evolution of the mean and turbulent structures of the planetary boundary layer. *Journal of the Atmospheric Sciences*, *35*(10), 1861–1883. https://doi.org/10.1175/1520-0469(1978)035<1861:mtheot>2.0.co;2

Arabas, S., Axelsen, S., Attema, J., Azizi, V., Beets, C., Boeing, S. J., et al. (2024). Dalesteam/dales: Dales 4.4.2. *Zenodo*. https://doi.org/10.5281/zenodo.11479354

Bougeault, P. (1981). Modeling the trade-wind cumulus boundary layer. Part ii: A high-order one-dimensional model. *Journal of the Atmospheric Sciences*, *38*(11), 2429–2439. https://doi.org/10.1175/1520-0469(1981)038<2429:mttwcb>2.0.co;2

Bretherton, C. S., MacVean, M. K., Bechtold, P., Chlond, A., Cotton, W. R., Cuxart, J., et al. (1999). An intercomparison of radiatively-driven entrainment and turbulence in a smoke cloud, as simulated by different numerical models. *Quarterly Journal of the Royal Meteorological Society*, *54*, 148–167.

Brown, A. R., Beljaars, A. C. M., & Hersbach, H. (2006). Errors in parametrizations of convective boundary-layer turbulent momentum mixing. *Quarterly Journal of the Royal Meteorological Society*, *132*(619), 1859–1876. https://doi.org/10.1256/qj.05.182

Brown, A. R., & Grant, A. L. M. (1997). Non-local mixing of momentum in the convective boundary layer. *Boundary-Layer Meteorology*, *84*, 1–22. https://doi.org/10.1023/a:1000388830859

Deardorff, J. W. (1973). Three-dimensional numerical modeling of the planetary boundary layer. In D. A. Haugen (Ed.), *Workshop on micrometeorology* (pp. 271–311). Amer. Met. Soc.

Deardorff, J. W. (1980). Stratocumulus-capped mixed layers derived from a three-dimensional model. *Boundary-Layer Meteorology*, *18*(4), 495–527. https://doi.org/10.1007/bf00119502

De Roode, S. R. (2007). The role of eddy diffusivity profiles on stratocumulus liquid water path biases. *Monthly Weather Review*, *135*(7), 2786–2793. https://doi.org/10.1175/mwr3426.1

De Roode, S. R., & Bretherton, C. S. (2003). Mass-flux budgets of shallow cumulus clouds. *Journal of the Atmospheric Sciences*, *60*(1), 137–151. https://doi.org/10.1175/1520-0469(2003)060<0137:mfbosc>2.0.co;2

De Roode, S. R., Frederikse, T., Siebesma, A. P., Ackerman, A. S., Chylik, J., Field, P. R., et al. (2019). Turbulent transport in the gray zone: A large eddy model intercomparison study of the constrain cold air outbreak case. *Journal of Advances in Modeling Earth Systems*, *11*(3), 597–623. https://doi.org/10.1029/2018ms001443

De Roode, S. R., Jansson, F., Mak, H. Y. L., & Nuijens, L. (2024). *Countergradient momentum transport in turbulent atmospheric boundary layers*. Authorea Preprints.

De Roode, S. R., Jonker, H. J., van de Wiel, B. J., Vertregt, V., & Perrin, V. (2017). A diagnosis of excessive mixing in Smagorinsky subfilter-scale turbulent kinetic energy models. *Journal of the Atmospheric Sciences*, *74*(5), 1495–1511. https://doi.org/10.1175/JAS-D-16-0212.1

De Roode, S. R., Jonker, H. J. J., Duynkerke, P. G., & Stevens, B. (2004). Countergradient fluxes of conserved variables in the clear convective and stratocumulus-topped boundary layer: The role of the entrainment flux. *Boundary-Layer Meteorology*, *112*(1), 179–196. https://doi.org/10.1023/b:boun.0000020167.25780.16

De Roode, S. R., & Siebesma, A. P. (2020). A bound on Ekman pumping. *Journal of Advances in Modeling Earth Systems*, *12*(3), e2019MS001976. https://doi.org/10.1029/2019ms001976

De Rooy, W. C., Siebesma, P., Baas, P., Lenderink, G., De Roode, S. R., De Vries, H., et al. (2022). Model development in practice: A comprehensive update to the boundary layer schemes in HARMONIE-AROME cycle 40. *Geoscientific Model Development*, *15*(4), 1513–1543. https://doi.org/10.5194/gmd-15-1513-2022

Deser, C. (1993). Diagnosis of the surface momentum balance over the tropical Pacific Ocean. *Journal of Climate*, *6*(1), 64–74. https://doi.org/10.1175/1520-0442(1993)006<0064:dotsmb>2.0.co;2

Dixit, V., Nuijens, L., & Helfer, K. C. (2021). Counter-gradient momentum transport through subtropical shallow convection in ICON-LEM simulations. *Journal of Advances in Modeling Earth Systems*, *13*(6), e2020MS002352. https://doi.org/10.1029/2020ms002352

ECMWF. (2023). *Ifs documentation cy48r1—Part IV: Physical processes*. Author. https://doi.org/10.21957/02054f0fbf

Frech, M., & Mahrt, L. (1995). A two-scale mixing formulation for the atmospheric boundary layer. *Boundary-Layer Meteorology*, *73*(1–2), 91–104. https://doi.org/10.1007/bf00708931

Heinze, R., Mironov, D., & Raasch, S. (2015). Second-moment budgets in cloud topped boundary layers: A large-eddy simulation study. *Journal of Advances in Modeling Earth Systems*, *7*(2), 510–536. https://doi.org/10.1002/2014ms000376

Helfer, K. C., Nuijens, L., & Dixit, V. V. (2021). The role of shallow convection in the momentum budget of the trades from large-eddy-simulation hindcasts. *Quarterly Journal of the Royal Meteorological Society*, *147*(737), 2490–2505. https://doi.org/10.1002/qj.4035

Heus, T., van Heerwaarden, C. C., Jonker, H. J. J., Siebesma, A. P., Axelsen, S., van den Dries, K., et al. (2010). Formulation of the Dutch Atmospheric large-eddy simulation (DALES) and overview of its applications. *Geoscientific Model Development*, *3*(2), 415–444. https://doi.org/10.5194/gmd-3-415-2010

Holtslag, A. A. M., & Moeng, C.-H. (1991). Eddy diffusivity and countergradient transport in the convective atmospheric boundary layer. *Journal of the Atmospheric Sciences*, *48*(14), 1690–1698. https://doi.org/10.1175/1520-0469(1991)048<1690:edacti>2.0.co;2

Honnert, R., Masson, V., & Couvreux, F. (2011). A diagnostic for evaluating the representation of turbulence in atmospheric models at the kilometric scale. *Journal of the Atmospheric Sciences*, *68*(12), 3112–3131. https://doi.org/10.1175/jas-d-11-061.1

Lappen, C.-L., & Randall, D. A. (2006). Parameterization of pressure perturbations in a pbl mass-flux model. *Journal of the Atmospheric Sciences*, *63*(7), 1726–1751. https://doi.org/10.1175/jas3722.1

Larson, V. E., Domke, S., & Griffin, B. M. (2019). Momentum transport in shallow cumulus clouds and its parameterization by higher-order closure. *Journal of Advances in Modeling Earth Systems*, *11*(11), 3419–3442. https://doi.org/10.1029/2019ms001743

Lilly, D. (1968). Models of cloud-topped mixed layers under a strong inversion. *Quarterly Journal of the Royal Meteorological Society*, *94*(401), 292–309. https://doi.org/10.1002/qj.49709440106

Park, S.-B., Böing, S., & Gentine, P. (2018). Role of surface friction on shallow nonprecipitating convection. *Journal of the Atmospheric Sciences*, *75*(1), 163–178. https://doi.org/10.1175/jas-d-17-0106.1

Pino, D., Vilà-Guerau de Arellano, J., & Duynkerke, P. G. (2003). The contribution of shear to the evolution of a convective boundary layer. *Journal of the Atmospheric Sciences*, *60*(16), 1913–1926. https://doi.org/10.1175/1520-0469(2003)060<1913:tcostt>2.0.co;2

Randall, D. A., Shao, Q., & Moeng, C.-H. (1992). A second-order bulk boundary-layer model. *Journal of the Atmospheric Sciences*, *49*(20), 1903–1923. https://doi.org/10.1175/1520-0469(1992)049<1903:asobbl>2.0.co;2

Salesky, S. T., Chamecki, M., & Bou-Zeid, E. (2017). On the nature of the transition between roll and cellular organization in the convective boundary layer. *Boundary-Layer Meteorology*, *163*(1), 41–68. https://doi.org/10.1007/s10546-016-0220-3

Sandu, I., Bechtold, P., Nuijens, L., Beljaars, A., & Brown, A. (2020). On the causes of systematic forecast biases in near-surface wind direction over the oceans. In *ECMWF technical memo*. ECMWF.

Sandu, I., Beljaars, A., Bechtold, P., Mauritsen, T., & Balsamo, G. (2013). Why is it so difficult to represent stably stratified conditions in numerical weather prediction NWP models? *Journal of Advances in Modeling Earth Systems*, *5*(2), 117–133. https://doi.org/10.1002/jame.20013

Siebesma, A. P., Soares, P. M. M., & Teixeira, J. (2007). A combined eddy-diffusivity mass-flux approach for the convective boundary layer. *Journal of the Atmospheric Sciences*, *64*(4), 1230–1248. https://doi.org/10.1175/JAS3888.1

Smagorinsky, J. (1963). General circulation experiments with the primitive equations: I. The basic experiment. *Monthly Weather Review*, *91*(3), 99–164. https://doi.org/10.1175/1520-0493(1963)091<0099:gcewtp>2.3.co;2

Smagorinsky, J., Manabe, S., & Holloway Jr, J. L. (1965). Numerical results from a nine-level general circulation model of the atmosphere. *Monthly Weather Review*, *93*(12), 727–768. https://doi.org/10.1175/1520-0493(1965)093<0727:nrfanl>2.3.co;2

Stevens, B., Ackerman, A. S., Albrecht, B. A., Brown, A. R., Chlond, A., Cuxart, J., et al. (2001). Simulations of trade wind cumuli under a strong inversion. *Journal of the Atmospheric Sciences*, *58*(14), 1870–1891. https://doi.org/10.1175/1520-0469(2001)058<1870:sotwcu>2.0.co;2

Stevens, B., Duan, J., McWilliams, J. C., Münnich, M., & Neelin, J. D. (2002). Entrainment, Rayleigh friction, and boundary layer winds over the tropical Pacific. *Journal of Climate*, *15*(1), 30–44. https://doi.org/10.1175/1520-0442(2002)015<0030:erfabl>2.0.co;2

Stull, R. B. (1988). *An introduction to boundary layer meteorology*. Kluwer Academic Publishers.666.

Sullivan, P. P., & Patton, E. G. (2011). The effect of mesh resolution on convective boundary layer statistics and structures generated by large-eddy simulation. *Journal of the Atmospheric Sciences*, *68*(10), 2395–2415. https://doi.org/10.1175/jas-d-10-05010.1

Svensson, G., & Holtslag, A. A. (2009). Analysis of model results for the turning of the wind and related momentum fluxes in the stable boundary layer. *Boundary-Layer Meteorology*, *132*(2), 261–277. https://doi.org/10.1007/s10546-009-9395-1

Teixeira, J., Suselj, K., & Kurowski, M. J. (2023). An introduction to the eddy–diffusivity/mass–flux (EDMF) approach: A unified turbulence and convection parameterization. In *Fast processes in large-scale atmospheric models: Progress, challenges, and opportunities* (pp. 271–282).

VanZanten, M. C., Duynkerke, P. G., & Cuijpers, J. W. M. (1999). Entrainment parameterization in convective boundary layers. *Journal of the Atmospheric Sciences*, *56*(6), 813–828. https://doi.org/10.1175/1520-0469(1999)056<0813:epicbl>2.0.co;2

Vreugdenhil, C. B., & Koren, B. (1993). Notes on numerical fluid mechanics. In *Numerical methods for advection-diffusion problems* (Vol. 45, p. 373). Vieweg.